41st Aerospace Sciences Meeting and Exhibit
6-9 January 2003, Reno, Nevada

AIAA 2003-497

FEASIBLILITY STUDY OF A LASER RAMJET SINGLE-STAGE-TO-ORBIT VEHICLE

Hiroshi KATSURAYAMA*, Yasuro HIROOKA†, Kimiya KOMURASAKI‡, and Yoshihiro ARAKAWA§

ABSTRACT

Momentum coupling coefficients, $C_{\rm m}$, of a laser ramjet vehicle are calculated by CFD and an engine cycle analysis. The flight trajectory of the laser ramjet vehicle is calculated by the engine cycle analysis. The CFD with the explosion source model can reproduce the experimental data of $C_{\rm m}$. Using this CFD model, $C_{\rm m}$ in a supersonic flight are computed. The results show $C_{\rm m}$ and the fraction of laser energy, that is converted to blast wave energy, decreases with the flight altitude due to chemically frozen flow loss. $C_{\rm m}$ by the engine cycle analysis is underestamted in comparsion with CFD. Since the engine cycle analysis is assumed to be steady state process, the peak pressure in the Humphery cycle is lower than CFD. Accordingly, the Humphrey cycle efficiency of the engine cycle analysis is degraded. This low efficiency of the cycle causes the small $C_{\rm m}$ of the engine cycle analysis.

NOMENCLATURE

A = cross section of a vehicle
$A_{\rm L}$ = cross section of laser beam
$C.A.R.$ = capture area ratio
$C_{\rm d}$ = drag coefficient
$C_{\rm m}$ = momentum coupling coefficient
$C_{\rm p}$ = specific heat at constant pressure
e = total energy per unit volume
$E_{\rm L}$ = total laser energy
$E_{\rm B}$ = the pressure and kinetic energy converted from the laser energy (Blast wave energy)
F = thrust
g = acceleration of gravity
H = flight altitude of the vehicle
h = enthalpy
$h^{\rm t+r}$ = sum of translational and rotational enthalpy
j = mass diffusion flux
f = f number of optics
M = Mach number
$m_{\rm v}$ = vehicle mass
$\dot{m}$ = mass flow rate
$P_{\rm L}$ = laser power
p = static pressure
q = heat flux
R = gas constant
V_0 = explosion source volume
S = maximum cross section of the vehicle
T = static temperature
t = time
U = vehicle speed
u, v = axial, radial velocity component
z, r, θ = cylindrical coordinates
γ = specific heat ratio
Δh^f = chemical potential energy
ϵ = structure coefficient
$\eta_{\rm d}$ = diffuser efficiency
η_B = blast wave efficiency to the blast wave energy
$\pi_{\rm d}$ = total pressure ratio
ρ = density
τ = viscous stress tensor

subscripts
i = inlet
s = species
t = stagnation condition
∞ = freestream property

INTRODUCTION

There is a strong demand to frequently deliver payloads to a space station at a low cost. A pulse laser ramjet vehicle will be able to satisfy this demand: Since energy is provided from a laser base on the ground to the vehicle and the atmospheric air can be used as a propellant, the payload ratio is improved drastically. In addition, once a laser base is constructed, the cost is only electricity charges.

The pulse laser ramjet vehicle as shown in Fig.1 will be able to achieve SSTO by switching its flight mode. Firstly, when the vehicle is launched from the ground, the inlet is closed to prevent the blast wave from going upstream beyond the inlet. Air is taken and exhausted from the rear side of the vehicle. This flight mode can be called a pulsejet mode. Secondly, when the vehicle is enough accelerated that the inflow air becomes free from thermal choking by laser heating, the inlet is open and the flight mode is switched to a ramjet mode. Finally, when the vehicle can not breath the enough air at high altitude, the flight mode is switched to a rocket mode.

*Graduate student, Department of Aeronautics and Astronautics, Student Member AIAA
†Graduate student, Department of Aeronautics and Astronautics
‡Associate Professor, Department of Advanced Energy, Member AIAA
§Professor, Department of Aeronautics and Astronautics, Member AIAA

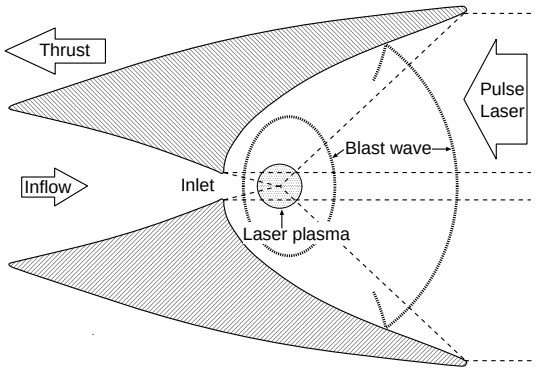

Fig.1 Pulse laser ramjet vehicle.

Air-breakdown occurs by focusing a transmitted pulse laser beam by the nozzle wall. The front of produced plasma absorbs the following part of laser pulse and expands in the form of Laser Supported Detonation wave (LSD).[1] This expansion induces a blast wave. The blast wave imparts the thrust to the nozzle wall.

Myrabo et al. proposed a pulse laser vehicle, named "Lightcraft," and conducted flight tests with a scaled model.[2] Their latest model, with additional solid ablative propellants, recorded the launch altitude of 121-meters.[3] Wang et al.[4] computed the flow field in the Lightcraft resting on the ground.

The objective of this paper is to analytically examine the feasibility of the laser ramjet SSTO vehicle. The launch trajectory is calculated by an engine cycle Analysis. Since there is not adequate investigation about the supersonic flight so far, and an experiment is difficult under the supersonic flight, the momentum coupling coefficient is computed by CFD. Finally, $C_{\rm m}$ deduced by the engine cycle analysis is compared with $C_{\rm m}$ by CFD.

MOMENTUM COUPLING AND BLAST WAVE EFFICIENCY

In the laser propulsion, the momentum coupling coefficient $C_{\rm m}$ is an performance indicator. $C_{\rm m}$ is the ratio of cumulative impulse to one pulse laser energy and defined as,

$$C_{\rm m} = \frac{\int_0^t F dt}{E_{\rm L}}. \tag{1}$$

The absorbed laser energy is converted into the blast wave energy $E_{\rm B}$, chemical potential energy and radiation energy. Since only energy, $E_{\rm B}$, is converted to the thrust, $C_{\rm m}$ would be function of $E_{\rm B}/E_{\rm L}$. We introduce the blast wave efficiency $\eta_{\rm B}$ defined by

$$\eta_{\rm B} = \frac{E_{\rm B}}{E_{\rm L}}. \tag{2}$$

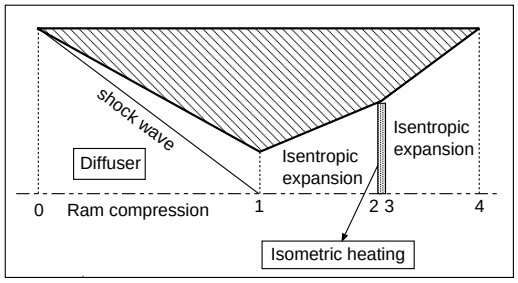

Fig.2 Ramjet engine cycle analyses.

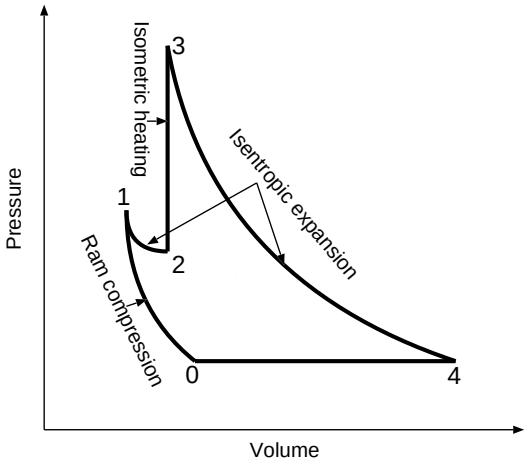

Fig.3 Humphrey cycle
(with additional isentropic expansion $1 \rightarrow 2$).

The flight trajectory is calculated using this $\eta_{\rm B}$ in a engine cycle analysis. In order to validate this analysis, the thrust is also computed by CFD.

ENGINE CYCLE ANALYSIS

Analysis Method

Pulsejet mode In a pulsejet mode, thrust is estimated using the experimental data of $C_{\rm m}$. $C_{\rm m}$ is assumed constant.

$$F = C_{\rm m} P_{\rm L} \tag{3}$$

Ramjet mode In a ramjet mode, thrust is calculated by an engine cycle analysis assuming Humphrey cycle[5] as indicated in Figs.2 and 3.

The area ratio is listed in Table 1. A_0 is defined as,

$$C.A.R. = \frac{\iint_{S_{\rm inlet}} \rho \boldsymbol{v} \cdot \boldsymbol{ds}}{\iint_{S_\infty} \rho \boldsymbol{v} \cdot \boldsymbol{ds}}, \tag{4}$$

$$A_0 = C.A.R. \times S. \tag{5}$$

From Point 0 to Point 1, air is ram-compressed. The total pressure ratio and total temperature are the followings,

$$\pi_{\rm d} = \frac{p_{\rm t1}}{p_{\rm t0}} = \left(1 + (1-\eta_{\rm d})\frac{\gamma-1}{2} M_0\right)^{-\frac{\gamma}{\gamma-1}} \tag{6}$$

$$T_{\rm t1} = T_{\rm t0}. \tag{7}$$

Table 1 Aera ratios.

S	A_0/S	A_1/S	$A_2/S = A_3/S$	A_4/S
$1\mathrm{m}^2$	0.6	0.38	0.75	1

η_d and γ are assumed as 0.97 and 1.4, respectively.

Then, M_1 is calculated by solving the following equation by Newton-Rapson method.

$$\frac{\left(2+(\gamma-1)M_1^2\right)^{\frac{\gamma+1}{2(\gamma-1)}}}{M_1} = \pi_\mathrm{d}\frac{A_1}{A_0}\frac{\left(2+(\gamma-1)M_0^2\right)^{\frac{\gamma+1}{2(\gamma-1)}}}{M_0}. \quad (8)$$

Density, temperature and pressure at Point 1 are calculated by M_1, $p_{\mathrm{t}1}$ and $T_{\mathrm{t}1}$.

From Point 1 to Point 2, air is isentropically expanded to prevent thermal choking by laser heating at the throat. The physical properties at location 2 are calculated by the Eqs. (6)$\sim$ (8) with $\pi_\mathrm{d} = 1$.

From Point 2 to Point 3, the air is isometrically heated. The physical properties at location 3 are calculated by mass conservation law and energy conservation law.

$$\rho_3 = \rho_2,\ u_3 = u_2,\ T_3 = T_2 + \frac{\eta_\mathrm{B}P_\mathrm{L}}{C_\mathrm{p}\dot{m}},$$
$$p_3 = \rho_2 R T_2,\ M_3 = u_3/\sqrt{\gamma R T_3}. \quad (9)$$

where Eq.(11) is used as $\eta_\mathrm{B}(\rho_2)$.

Finally, air is again isentropically expanded from Point 3 to Point 4, and the thrust is calculated as the following,

$$F = \dot{m}(u_4 - u_0) + A_4(p_4 - p_0). \quad (10)$$

Rocket mode As the vehicle reaches high altitudes in the ramjet mode, the mass flow rate decreases due to the low air density. In this calculation, the flight mode is switched from the ramjet mode to the rocket mode when the thermal choking occurs in the ramjet mode.

In the rocket mode, Point 1 is closed and H_2 fuel is injected between Point 1 and Point 2. The fuel is laser-heated from Point 2 to Point3 and the flow is assumed to choke thermally at Point 3. Since the energy of flow before laser-heating is negligibly small as compared with the input laser energy, the flowing relation is derived from the energy conservation law and the state equation,

$$T_3 = \frac{\eta_\mathrm{B}P_\mathrm{L}}{\dot{m}_\mathrm{p}}\left[\frac{2}{C_\mathrm{p}(\gamma+1)}\right], \quad (11)$$

$$p_3 = \frac{\dot{m}_\mathrm{p}}{A_3}\sqrt{\frac{RT_3}{\gamma}}. \quad (12)$$

From Point 3 to Point 4, the isentropic expansion is assumed, and the thrust is calculated by Eq.(18).

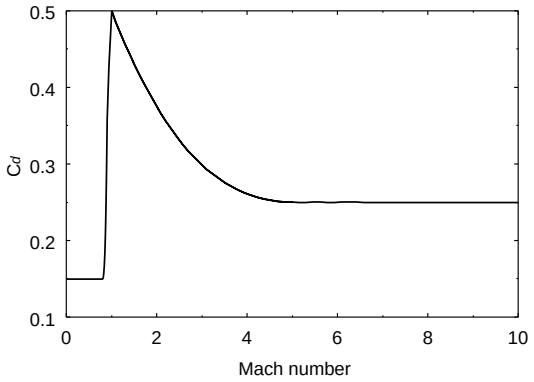

Fig.4 C_d used for the trajectory calculation.

The vehicle mass changes according to the injected fuel mass,

$$m_\mathrm{v}(t) = m_\mathrm{v}(0) - \int_0^t \dot{m}_\mathrm{p}dt. \quad (13)$$

Launch trajectory and payload ratio The vertical launch trajectory is calculated by solving the following motion equation by the 4th order Runge-Kutta scheme.

$$m_\mathrm{v}\frac{dU}{dt} = F - \frac{1}{2}\rho_\infty U^2 S C_\mathrm{d} - m_\mathrm{v}g \quad (14)$$

Herein, the flight condition is decided automatically by tracing the trajectory. The trajectory is calculated till the time, t_e, when the vehicle accelerates to the first cosmic velocity, 7.91 km/s. The payload ratio is estimated from the following,

$$m_\mathrm{p} = \int_{t_\mathrm{r}}^{t_\mathrm{e}} \dot{m}_\mathrm{p}dt, \quad (15)$$

$$\text{Payload ratio} = \frac{m_\mathrm{v}(0) - \frac{m_\mathrm{p}}{1-\epsilon}}{m_\mathrm{v}(0)} \quad (16)$$

where t_r is the time when the rocket mode starts.

Although ϵ must be about 0.25 to achieve SSTO by SCRamjet engine,[6] the structure weight of laser ramjet vehicle can be reduced due to the simple structure. In this calculation, ϵ is assumed to be 0.1.

SSTO Trajectory by Engine Cycle Analysis

Figure 5 show the Mach number vs. altitude diagram which is calculated under conditions tabulated in Table 2.

The mode switch from the pulsejet to the ramjet occurs at $M = 2.0$ and $H = 7$ km. C_m of the ramjet mode has the maximum value, 200 N/MW, at the point and then gradually decreases with the flight altitude owing to the decrease of mass flow rate.

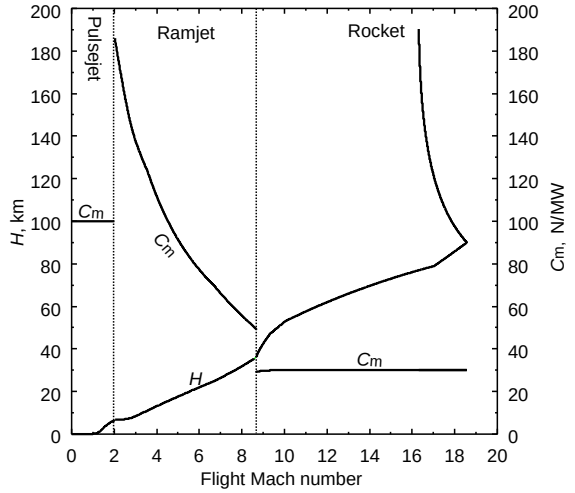

Fig.5 H, $C_{\rm m}$ Vs. M diagram.

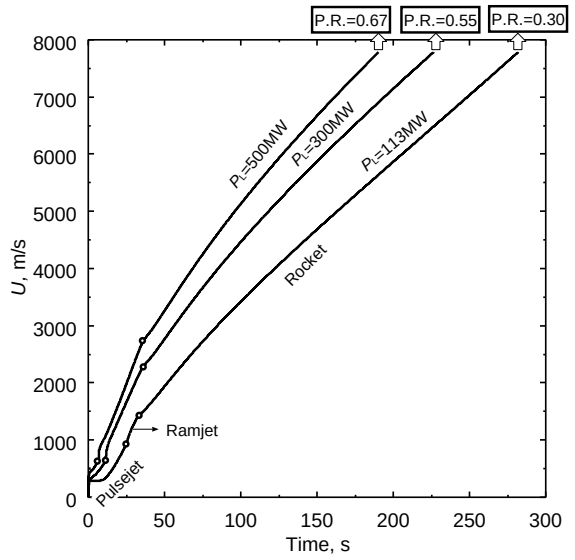

Fig.6 Flight velocity Vs. time diagram.

The mode switch from the ramjet to the rocket occurs at $M = 8.7$ and $H = 36$ km where $C_{\rm m}$ of the ramjet is 49 N/NW. In the rocket mode, $C_{\rm m}$ is almost constant value, 30 N/MW.

Figure 6 shows payload ratios for $P_{\rm L}$ = 113, 300 and 500MW, where the parameters except $P_{\rm L}$ is the same as Table 2.

Table 2 Calculation conditions in engine cycle analysis.

$m_{\rm v}\,(t=0)$	100 kg
$P_{\rm L}$	500 MW
$\eta_{\rm B}$	40 %
$C_{\rm m}^{\rm (pulsejet)}$	100 N/MW
$\dot{m}_{\rm p}$	1 kg/s
$\eta_{\rm d}$	0.97
ϵ	0.1

CFD ANALYSIS

Governing Equations

Axisymmetric Navier-Stokes equations are solved. Chemical reactions are treated as finite rate reactions. The following 11 species of air plasma are considered: N_2, O_2, NO, N, O, N_2^+, O_2^+, NO^+, N^+, O^+ and e^-. The effects of thermal non-equilibrium and radiative energy transfer are not considered. Then, the governing equations are given by

$$\frac{\partial \mathbf{U}}{\partial t}+\frac{\partial \mathbf{F}}{\partial z}+\frac{1}{r}\frac{\partial r\mathbf{G}}{\partial r}=\frac{\partial \mathbf{F_v}}{\partial z}+\frac{1}{r}\frac{\partial r\mathbf{G_v}}{\partial r}+\frac{\mathbf{H}}{r}+\mathbf{S}. \tag{17}$$

$$\mathbf{U}=\begin{bmatrix}\rho\\ \rho u\\ \rho v\\ e\\ \rho_1\\ \vdots\\ \rho_{11}\end{bmatrix},\mathbf{F}=\begin{bmatrix}\rho u\\ \rho u^2+p\\ \rho uv\\ (e+p)\,u\\ \rho_1 u\\ \vdots\\ \rho_{11}u\end{bmatrix},\mathbf{G}=\begin{bmatrix}\rho v\\ \rho uv\\ \rho v^2+p\\ (e+p)\,v\\ \rho_1 v\\ \vdots\\ \rho_{11}v\end{bmatrix},$$

$$\mathbf{F_v}=\begin{bmatrix}0\\ \tau_{zz}\\ \tau_{zr}\\ u\tau_{zz}+v\tau_{zr}+q_z\\ j_{1z}\\ \vdots\\ j_{11z}\end{bmatrix},\mathbf{G_v}=\begin{bmatrix}0\\ \tau_{zr}\\ \tau_{rr}\\ u\tau_{zr}+v\tau_{rr}+q_r\\ j_{1r}\\ \vdots\\ j_{11r}\end{bmatrix},$$

$$\mathbf{H}=\begin{bmatrix}0\\ 0\\ p-\tau_{\theta\theta}\\ 0\\ 0\\ \vdots\\ 0\end{bmatrix},\mathbf{S}=\begin{bmatrix}0\\ 0\\ 0\\ 0\\ \omega_1\\ \vdots\\ \omega_{11}\end{bmatrix}. \tag{18}$$

E and the equation of state are defined as

$$E = \sum_{11}\rho_s h_s\,(T)-p+\frac{\rho\left(u^2+v^2\right)}{2}, \tag{19}$$

$$p = \sum_{11}\rho_s R_s T. \tag{20}$$

h_s and the transport properties are taken from Ref. (7) In the air chemical reaction model, the forward rates of Ref. (8) are used. The backward rates are calculated by the principle of detailed balance. The chemical equilibrium constants are also taken from Ref. (8).

Numerical Scheme

Inviscid flux is estimated with the AUSM-DV scheme[9] and space accuracy is extended to 3rd-order by the MUSCL approach with Edwards's pressure limiter.[10] Viscous flux is estimated with a standard central difference. Time integration is performed with the LU-SGS[11] scheme which is extended to 3rd-order time accuracy by Matsuno's inner iteration method.[12] The calculation is performed with the CFL number of $2 \sim 20$.

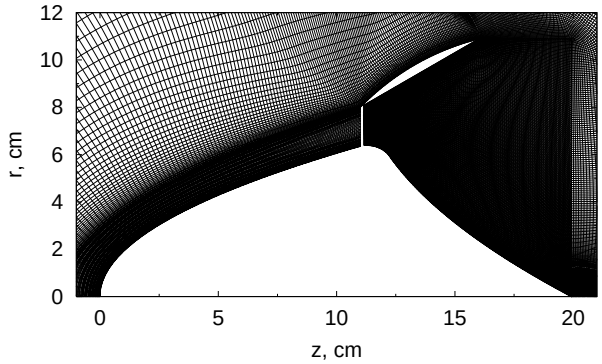

(a) Type A : 30° slope cowl (inlet is closed.)

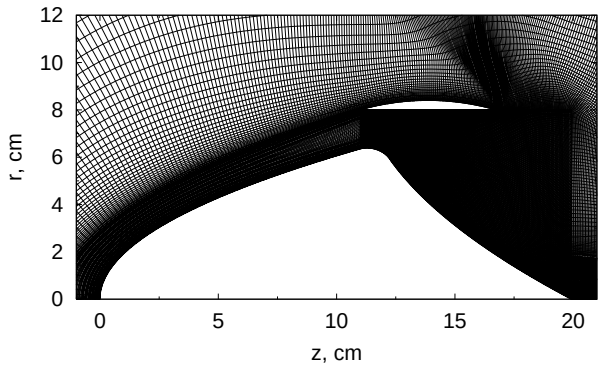

(b) Type B : non-slope cowl (inlet is open.)

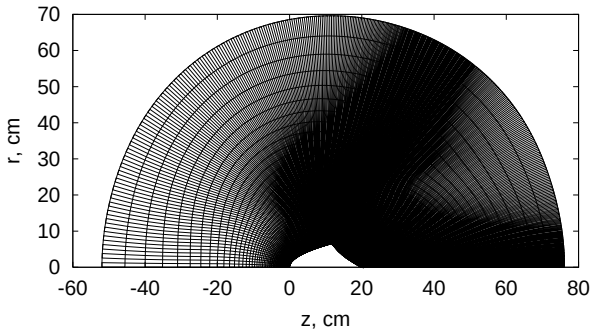

(c) Overall mesh (72,000 cells)

Fig.7 Computational mesh

Computational Mesh and Flight Condition

Figures 7 (a) $\sim$ (c) show computational meshes. Type A vehicle is used in the pulsejet mode. This is almost the same as the "Label E" Lightcraft.[2)] The computed $C_{\rm m}$ is compared with the experimental $C_{\rm m}$ data to validate this computation. Type B vehicle with a non-slope cowl is used in the ramjet mode since $C_{\rm d}$ of Type B is half of Type A.

The mesh cells are set to be fine between the cowl and body to correctly capture a blast wave. In addition, the mesh is concentrated near the wall to resolve the viscous boundary layer. The mesh width in the vicinity of the wall is $\Delta y = 80\mu$m. The outer boundary of the computational zone is set far from the vehicle body to reduce the influence of non-physical reflection waves from the outer boundary.

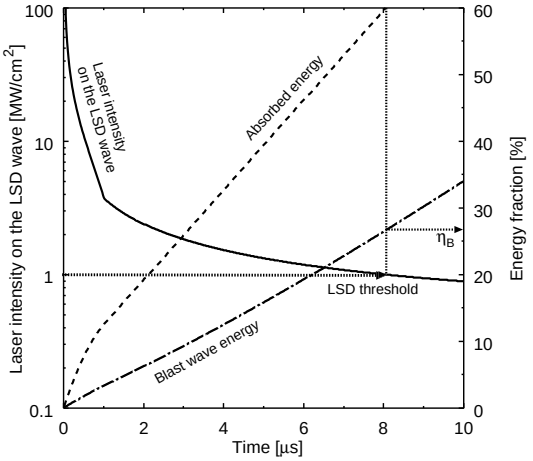

Fig.8 Histories of $E_{\rm B}$ and laser intensity at $H =$ 0km.

The mesh convergence of $C_{\rm m}$ at $H = 0$km is checked with doubly divided cells.

Table 3 Mesh convergence of $C_{\rm m}$ at $H = 0$km.

Cell number	$C_{\rm m}, N/MW$
72,000	107
288,000	104

Since the difference is only 3 %, the 72,000 cells are used in this computation.

For a supersonic flight, the following conditions is chosen from the calculated trajectory.

Table 4 Supersonic flight condition.

H, km	M	p_∞, atm	ρ_∞, kg/m^3
20	5	0.055	0.089

Explosion Source Model

A explosion source model[13)] is employed instead of solving complex propagation processes of LSD wave: The explosion source is modeled as a pressurized volume centered at the laser focus. The blast wave is driven by burst of this source. The focus is located at the middle on the inner cowl surface. Since LSD processes can be considered as isometric heating,[1)] the density in the source is assumed to be invariant during the heating process. The source is assumed to be in chemical equilibrium. The chemical composition is calculated by the method in Ref. (14).

One Dimensional LSD Analysis

In order to model the explosion source, 1-D LSD propagation process is calculated. From three con-

servation equations and C-J condition, the the following relations are derived.[15)]

$$p_2 = \frac{p_1 + \rho_1 D_{\rm CJ}^2}{\gamma_2 + 1}, \quad (21)$$

$$\rho_2 = \frac{(\gamma_2 + 1)\,\rho_1 D_{\rm CJ}^2}{\gamma_2\,(p_1 + \rho_1 D_{\rm CJ}^2)}, \quad (22)$$

$$T_2 = p_2/R_2/\rho_2, \quad (23)$$

$$v_2 = c_2 = \sqrt{\frac{\gamma_2 p_2}{\rho_2}}, \quad (24)$$

$$v_1 = D_{\rm CJ}, \quad (25)$$

$$h_2 = h_1 + \frac{1}{2}\left(D_{\rm CJ} - v_2^2\right) + \frac{P_{\rm L}/A_{\rm L}}{\rho_1 D_{\rm CJ}}, \quad (26)$$

where the subscripts 1 and 2 denote the states in front of and behind the LSD wave, respectively. The velocities refer the coordinate relative to the LSD wave. Since the laser beam is focused cylindrically as shown in Fig.7,

$$A_{\rm L} = 2\pi\,(r_{\rm f} - r_{\rm d})\tan^{-1}(f)\,.$$

Here, $r_{\rm f}$ and $r_{\rm d}$ are the radius of the focus and the detonation wave front, respectively. f is 3.6.[2)] The history of $P_{\rm L}$ is taken from the Ref. (16).

The Eqs. (3) $\sim$ (8) are iteratively solved with chemical equilibrium calculation. Then, the location of LSD is calculated by

$$\frac{dr_{\rm d}}{dt} = D_{\rm CJ}. \quad (27)$$

In an atmospheric pressure, CO_2 laser intensity below 1MW can not sustain LSD wave.[17)] In the present computation, the laser absorption is assumed to finish when laser intensity on the LSD wave decays to this threshold. $E_{\rm B}$ is defined as the sum of kinetic energy at $t = t_{\rm l}$ when $P_{\rm L}/A_{\rm L} = 1$ MW/cm^2,

$$E_{\rm B} = \int_0^{t_{\rm l}} \left[h_2^{\rm t+r} - h_1^{\rm t+r} + \frac{1}{2}(D_{\rm CJ} - v_2)^2\right]\rho_1 D_{\rm CJ} A_{\rm L}\,dt. \quad (28)$$

Figure 8 shows the history of the laser intensity, and absorbed laser energy and blast wave energy. When laser intensity on the LSD wave decays to LSD threshold, 60 % of laser energy is absorbed by plasma and 26 % of laser energy is converted to blast wave energy. Table 5 shows the source volume decided by this $\eta_{\rm B}$. The blast wave is driven at $t_0 = 0$ μs by burst of this source volume.

Table 5 Explosion source.

H, km	$E_{\rm L}$, J	$\eta_{\rm B}\,(t_0)$, %	V, cm^3
0	400	26.0	17.4
20	300	18.8	44.4
	400	17.2	51.3
	500	16.1	55.6

where the absorption fraction of laser energy is assumed to be constant, 60 %, because the LSD threshold is unknown in reduced atmospheric density.

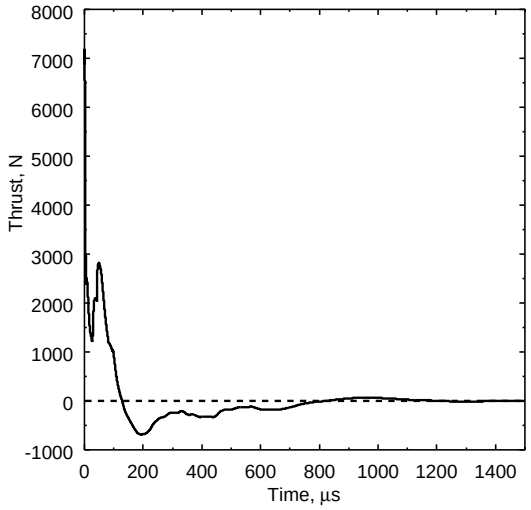

Fig.9 Thrust history

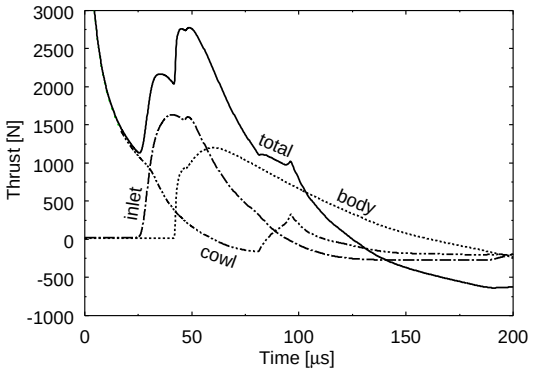

Fig.10 Each thrust received by body, cowl and closed inlet

Computed Results at $H = 0$ km

A blast wave is driven at $H = 0$km by the explosion source in Table 5. The history of axial thrust is shown in Fig.9. After the positive thrust maintains till 125 μs, the negative thrust continues till 900 μs. After 1500 μs, the thrust almost is equal to zero.

Figure 10 shows the thrust received by the body, cowl and closed inlet till 200 μs. After the explosion source bursts at t_0, the shock wave expands suddenly and decays. Therefore, the thrust received by the cowl decreases fast.

The thrust received by the closed inlet and the afterbody decreases slower than that of the cowl.

Figures 11 (a) $\sim$ (c) shows the propagation processes of the shock wave. The shock wave starts to sweep on the afterbody at $t_1 = 45\mu$s. The shock wave propagates beyond the middle of the after-

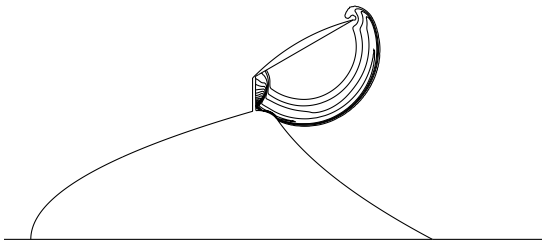

(a) At $t_1 = 45\mu$s
($p_{\max} = 6.71$atm, $p_{\min} = 0.77$atm, $dp = 0.30$atm)

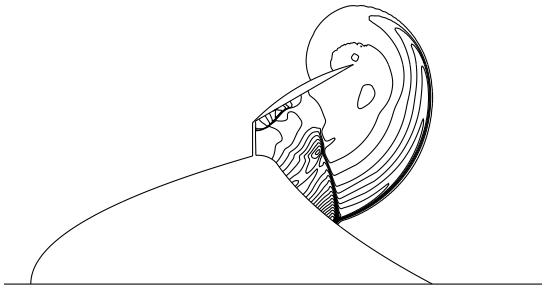

(b) At $t_2 = 100\mu$s
($p_{\max} = 3.86$atm, $p_{\min} = 0.52$atm, $dp = 0.17$atm)

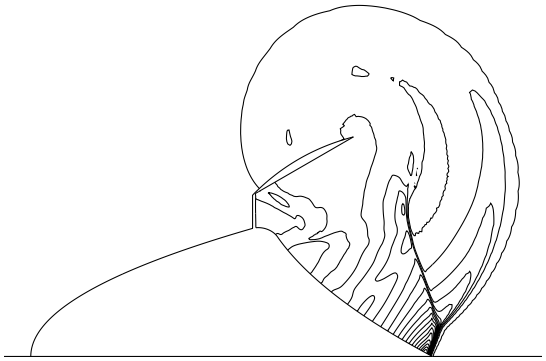

(b) At $t_3 = 190\mu$s
($p_{\max} = 3.54$atm, $p_{\min} = 0.75$atm, $dp = 0.14$atm)

Fig.11 Pressure contours in $H = 0$ km.

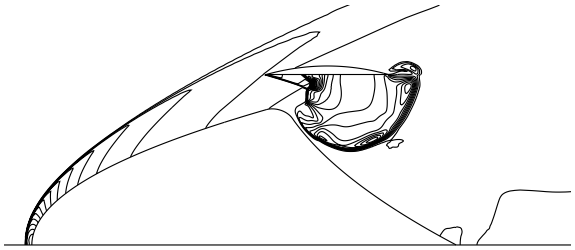

(a) At $t = 12\mu$s.
($p_{\max} = 2.27$atm, $p_{\min} = 2.1 \times 10^{-2}$atm, $dp = 0.11$atm)

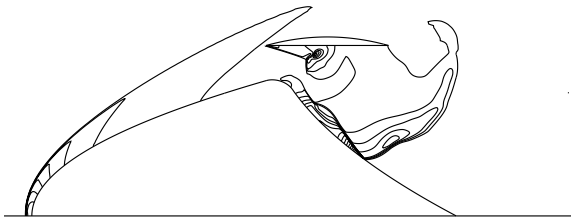

(b) At $t = 20\mu$s.
($p_{\max} = 4.63$atm, $p_{\min} = 2.1 \times 10^{-2}$atm, $dp = 0.23$atm)

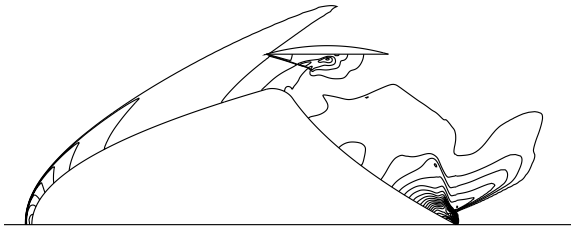

(c) At $t = 38\mu$s.

($p_{\max} = 4.27$atm, $p_{\min} = 2.0 \times 10^{-2}$atm, $dp = 0.21$atm)

Fig.12 Pressure contours after an explosion with $E_{\rm L} = 400$J at $H = 20$km and $M = 5$.

body at $t_2 = 100\mu$s. Then, the shock wave leaves the afterbody tail at $t_3 = 190\mu$s.

The computed $C_{\rm m}$ agrees with the experimental data, as listed in Table 6.

Consequently, this computational code with this physical modeling is found to reproduce the experimental data.

Table 6 Comparison of $C_{\rm m}$ at $H = 0$km.

Vehicle name	$C_{\rm m}$, N/MW
Label E (Ref. (2))	100
Type A (present)	107

Computed Results at H=20 km

Figures 12 (a) $\sim$ (b) show pressure contours after an explosion with $E_{\rm L} = 400$J at $H = 20$km and $M = 5$. The blast wave sweeps the afterbody from the inlet from $t = 12\mu$s to 38μs, without being spat out from the inlet. Figure 13 shows the thrust histories. The blast wave speed of $H = 20$km case is faster than that of $H = 0$km case due to small ambient pressure and high speed inflow.

The computed $C_{\rm m}$, $\dot{m}$ and $C.A.R.$ are listed in:

Table 7 The computed $C_{\rm m}$ at $H = 20$km.

$E_{\rm L}$, J	$C_{\rm m}$, N/MW
300	67.9
400	64.8
500	61.8

Because $\eta_{\rm B}$ decreases with $E_{\rm L}$, $C_{\rm m}$ also decreases with $E_{\rm L}$.

Variation of $\eta_{\rm B}$ after Explosion

The time-variation of $\eta_{\rm B}$ is investigated. $E_{\rm B}$ is

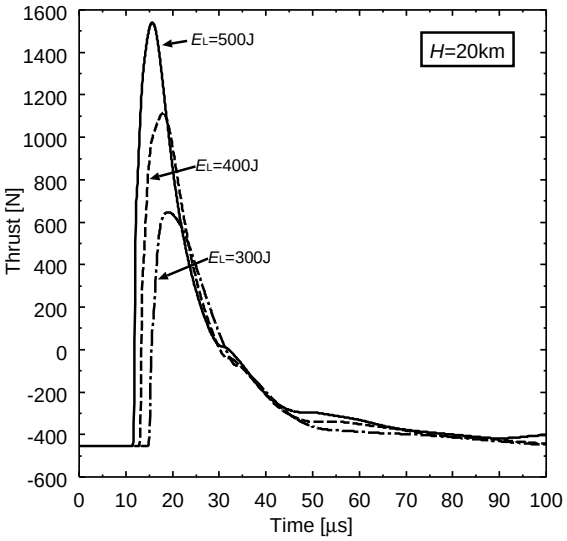

Fig.13 Thrust histories of $H = 20$km.

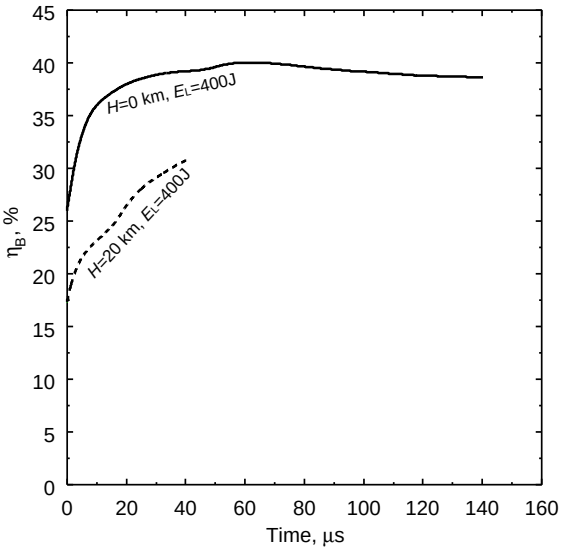

Fig.15 History of $\eta_{\rm B}$ in the case of $E_{\rm L} = 400$J.

integrated overall the computational zone such as,

$$E_{\rm B} = \int \left[\frac{p - p_0}{\gamma - 1} + \frac{\rho\left(u^2 + v^2\right) - \rho_0\left(u_0^2 + v_0^2\right)}{2} \right] dV. \quad (29)$$

The subscript 0 indicates the values before the explosion. Figure 15 shows the time variation of η_B from the just exploded time to the time when the blast wave finishes to sweep the afterbody. At $H = 0$km, $\eta_{\rm B}$ recovers due to the energy conversion from the chemical potential from $t = 0\mu$s to $t = 10\mu$s. After $t = 10\mu$s, the recovery rate decreases and the chemical potential energy is frozen.

At $H = 20$km, the blast wave finishes to sweep the afterbody before the recovery of $\eta_{\rm B}$ is completed. Consequently, large chemical energy is frozen. Since the chemically frozen loss increases with the atmospheric density, $C_{\rm m}$ decreases with the flight altitude.

DISCUSSION

In order to validate the engine cycle analysis, $C_{\rm m}$ of the engine cycle analysis are compared with $C_{\rm m}$ of CFD. The engine cycle analysis is conducted with the same flight conditions and vehicle cross sections as CFD. $\eta_{\rm B}$ of the engine cycle analysis are taken from the time-average value of CFD between the just exploded time and the time when the blast wave finishes to sweep the afterbody.

Table 8 $\eta_{\rm B}$ of the engine cycle analysis

$E_{\rm L}$, J	$\eta_{\rm B}$, %
300	26.6
400	25.9
500	24.9

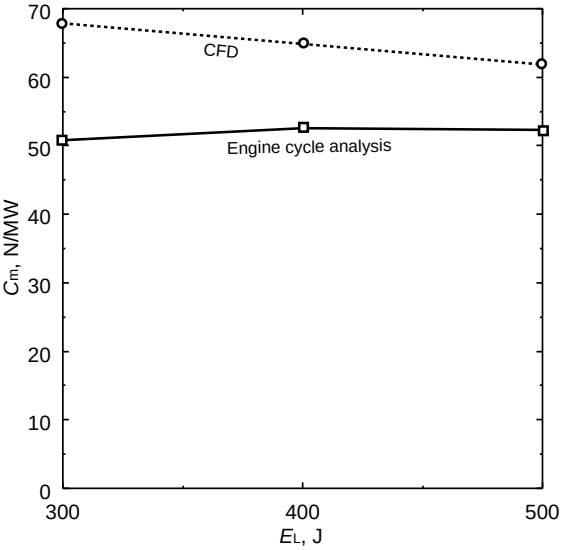

Fig.17 Comparison of $C_{\rm m}$ between CFD and the engine cycle analysis.

Fig.17 shows $C_{\rm m}$ of CFD and the engine cycle analysis. $C_{\rm m}$ of the engine cycle analysis are underestimated.

Since the engine cycle analysis is assumed to be steady state process, the peak pressure at Point 3 shown in Fig.3 is lower than CFD. Accordingly, the Humphrey cycle efficiency is degraded. This low efficiency of the cycle causes the small $C_{\rm m}$ of the engine cycle analysis.

In order correctly to estimate $C_{\rm m}$ by the engine cycle analysis, the unsteady effect should be incorporated to the cycle.

SUMMARY

The flight trajectory of the laser ramjet vehicle is calculated by the engine cycle analysis.

The CFD with the explosion source model can reproduce the experimental data of C_{m}. Using this CFD model, C_{m} in the supersonic flight is computed. The results show C_{m} and η_{B} decrease with the flight altitude due to chemically frozen flow loss.

C_{m} by the engine cycle analysis is underestimated in comparison with CFD. Since the engine cycle analysis is assumed to be steady state process, the peak pressure in the Humphrey cycle is lower than CFD. Accordingly, the Humphrey cycle efficiency of the engine cycle analysis is degraded. This low efficiency of the cycle causes the small C_{m} of the engine cycle analysis.

REFERENCES

1) Raizer, Y.P.: Laser-Induced Discharge Phenomena, Consultants Bureau, New York and London, 1977, Ch.6.

2) Myrabo, L.N., Messitt, D.G., and Mead, F.B.Jr.: Ground and Flight Tests of a Laser Propelled Vehicle, AIAA Paper 98-1001, 1998.

3) Myrabo, L.N.: World Record Flights of Beam-Riding Rocket Lightcraft: Demonstration of "Disruptive" Propulsion Technology Flight Tests of a Laser Propelled Vehicle, AIAA Paper 01-3798, 2001.

4) Wang, T.S., Mead, F.B.Jr., Larson, C.W.: Advanced Performance Modeling of Experimental Laser Lightcrafts, AIAA Paper 01-3664, 2001.

5) Bussing, T.R.A., and Pappas, G.: An Introduction to Pulse Detonation Engines, AIAA Paper 94-0263, 1994.

6) Shiramizu, M., Techincal Memorandum of National Aerospace Laboratory of Japan No.598, 1989.

7) Gupta, R.N., Yos, J.M., Thompson R.A. and Lee, K.P.: A Review of Reaction Rates and Thermodynamic and Transport Properties for an 11-Species Air Model for Chemical and Thermal Nonequilibrium Calculations to 30,000 K, NASA RP 1232, 1990.

8) Park, C.: Review of Chemical-Kinetic Problems of Future Flight NASA Missions, I: Earth Entries, Calculations to 30,000 K, *J. Thermophys. Heat Transfer*, **7** (1993), pp.385-398.

9) Wada, Y., and Liou, M.S. : A Flux Splitting Scheme with High-Resolution and Robustness for Discontinuities, NASA TM-106452, 1994.

10) Edwards, J.R. : A Low-Diffusion Flux-Splitting Scheme for Navier-Stokes Calculations, *Computers & Fluids*, **26** (1997), pp.635-659.

11) Jameson A., and Yoon, S. Lower-Upper Implicit Schemes with Multiple Grids for the Euler Equations, *AIAA Journal*,**25** (1987), pp.929-935.

12) Matsuno, K. : Actual Numerical Accuracy of an Iterative Scheme for Solving Evolution Equations with Application to Boundary-Layer Flow, *Trans. Japan Soc. Aero. Space. Sci.*, **38** (1996), pp.311-322.

13) Ritzel, D.V., and Matthews, K.: An adjustable explosion-source model for CFD blast calculations, *Proc. of 21st International Symposium on Shock Waves*, pp.97-102,1997.

14) Botton, B., Abeele, D.V., Carbonaro, M., and Degrez G.: Thermodynamic and Transport Properties for Inductive Plasma Modeling, *J. Thermophys. Heat Transfer*, **13** (1999), pp.343-350.

15) Landau, L.D. and Lifshitz, E.M.: Fluid Mechanics, 2nd ed., Butterworth-Heinemann, Oxford, 1987, Ch.14.

16) Messitt, D.G., Myrabo, L.N. and Mead, F.B.Jr.: Laser Initiated Blast Wave for Launch Vehicle Propulsion, AIAA 2000-3848, 2000.

17) Pirri, A.N., Root, R.G., and Wu, P.K.: Plasma Energy Transfer to Metal Surfaces Irradiated by Pulsed Lasers, *AIAA J.*, **16** (1978), pp.1296-1304.